

Wireless Infrared-based LiFi Uplink Transmission with Link Blockage and Random Device Orientation

Cheng Chen, *Member, IEEE*, Dushyantha A. Basnayaka, *Senior Member, IEEE*, Ardimas Andi Purwita, *Student Member, IEEE*, Xiping Wu, *Member, IEEE*, and Harald Haas, *Fellow, IEEE*

Abstract—Light-fidelity (LiFi) is recognised as a promising technology for next generation wireless access networks. However, limited research efforts have been spent on the uplink (UL) transmission system in LiFi networks. In this paper, a wireless infrared (IR)-based LiFi UL system is investigated. In particular, we focus on the performance of a single static user under the influence of random device orientation and link blockage. Simulations and mathematical analysis have been used to evaluate the UL system performance. The analytical expressions for the UL optical wireless channel and signal-to-noise ratio (SNR) statistics under the effects of random device orientation and link blockage are derived. The results show that the effects of random orientation and link blockage may lead to a decrease in coverage probability by 10% - 40% with various SNR thresholds.

Index Terms—Light-fidelity, optical wireless communication, uplink transmission, visible light communication, link blockage, device random orientation.

I. INTRODUCTION

WITH the already overcrowded radio frequency (RF) spectrum resources, it becomes more and more challenging to achieve wireless networks that can fulfil the increasing wireless data traffic demand. Consequently, wireless communications based on spectrum resources in the high frequency region have been considered. Visible light communication (VLC) is one of the most promising solutions. A VLC link is able to provide a data rate of more than 10 Gbps [1]. Based on VLC technology, a small-cell wireless access network, known as Light Fidelity (LiFi), has been proposed. Compared to VLC, a LiFi network is a unique and multifunctional system, which uses multiple coordinated light sources in an indoor environment as access points (APs). Each AP provides connectivity to a few nearby mobile users. A LiFi network is able to provide duplex transmission between an AP and user equipment (UE). It also supports multiple access, handover and many other useful functionalities [2]. Due to the fact that light signals are directional and cannot penetrate opaque objects, LiFi networks can provide more secure wireless connectivity in an indoor environment compared to conventional RF access networks [3]. In addition,

LiFi networks achieve a considerable increase in data rate per unit area, which makes LiFi advantageous over RF small-cells in densely populated scenarios [4].

In a number of survey publications, potential technologies for LiFi uplink (UL) have been discussed [5], with UL approaches using RF, VLC and wireless infrared (IR) being considered most frequently. A comparison between various existing RF technologies that can be used for LiFi UL has been presented in [6]. Wireless Fidelity (WiFi) or other RF technologies have been considered as the UL system in a RF-optical heterogeneous network [7]. Despite the convenience of using RF-based UL systems, they also introduce interference to existing RF systems. Furthermore, RF technologies cannot be used in electromagnetic interference (EMI)-sensitive areas. The use of VLC technology in the UL has been considered and experimentally demonstrated in [8], [9]. However, visible light UL signals may cause interference to the VLC-based downlink (DL) transmission. In addition, it also causes discomfort to the eyes of users. The propagation of a wireless IR signal is similar to that of a visible light signal, but the signal spectrum is in the IR region which is invisible to the human eye. Thus, it causes no discomfort to users. More importantly, it does not interfere with either RF or VLC-based systems. The use of IR-based UL have been demonstrated experimentally in a number of studies [10]–[13]. In particular, the achievable UL bit rates with various link distances and horizontal offset are measured in [10] and [11], respectively. The performance of IR-based UL systems with surveillance cameras used as UL detectors is evaluated in [12]. The optical power of UL IR-light-emitting diodes (LEDs) is lower compared to that of DL LEDs, which makes it more challenging to achieve a high signal-to-noise ratio (SNR) for an IR UL channel. Therefore, a few studies consider single carrier modulation schemes for UL transmission. These modulation schemes offer a low peak-to-average power ratio (PAPR) and low complexity on the user side [14], [15]. The IR-based UL transmission in an aircraft cabin environment has been investigated using simulations in [16]. The existing research on IR-based UL transmission considers the transmission performance of specific positions/orientations of LEDs/photodiodes (PDs). Many of these studies evaluate the link with a perfect LED-PD alignment. However, perfect alignment is unlikely in practical scenarios. In addition, IR signals cannot penetrate opaque objects, which means the IR-based link might be vulnerable to link blockage caused by human bodies. To alleviate issues arising from misalignment, an omnidirectional transmitter and receiver design for IR-based UL transmission has been proposed in [17]. An al-

Cheng Chen, Ardimas Andi Purwita and Harald Haas are with the LiFi Research and Development Centre, Institute for Digital Communications, The University of Edinburgh, EH9 3JL, Edinburgh, UK, e-mail: {cheng.chen, d.basnayaka, a.purwita, h.haas}@ed.ac.uk. Dushyantha A. Basnayaka is with School of Electronic Engineering, Dublin City University, Dublin 9, Ireland, e-mail: d.basnayaka@dcu.ie. Xiping Wu is with Department of Engineering Science, University of Oxford, OX1 3PJ, Oxford, UK, e-mail: xiping.wu@eng.ox.ac.uk

This work was supported by the Engineering and Physical Sciences Research Council (EPSRC) grant EP/L020009/1: Towards Ultimate Convergence of All Networks (TOUCAN).

ternative solution that uses a beam steering mechanism has been proposed in [18], which is further improved by using an angular diversity receiver (ADR) in [19]. Another multiple output system with a multi-face PD has been investigated in [20], but the authors focus on increasing the maximum number of supported users. Concerns about LiFi link channel uncertainty caused by random UE orientation and link blockage have been raised by many publications, but no study has conducted a dedicated investigation on this issue. In this paper, we focus on the performance of a LiFi wireless IR-based UL transmission under the effects of random device orientation and link blockage. The main contributions are concluded as follows:

- In order to improve the performance evaluation accuracy, we extend the optical wireless communication (OWC) transmission model based on pulse amplitude modulation with single carrier frequency domain equalisation (PAM-SCFDE) [21] to include the front-end low-pass characteristics and wavelength dependent characteristics.
- Due to the unique position/orientation of the receiver detector and the low optical power in the UL scenario, the noise properties are different from the case in the VLC DL scenario. Therefore, the noise characteristics in the UL scenario are simulated and discussed.
- A mathematical analysis on the statistics of the optical wireless channel and SNR under the effects of random device orientation and link blockage is presented. Closed-form expressions with a mathematical approximation is concluded.
- Coverage probabilities of the LiFi UL transmission with various AP deployments and association policies are evaluated. In addition, the effects and configurations of important parameters are discussed based on the evaluation results. In particular, the performance penalties caused by link blockage and random device orientation are highlighted.

Our results show that link blockage and random device orientation may have a significant effects on the performance of the UL transmission. This study offers researchers with a figure of LiFi UL performance in the practical scenario if a set of system parameters are provided. In addition, it can help researchers to develop advanced wireless IR-based UL systems or channel models.

The remainder of this paper is organised as follows: the wireless IR UL system model and the evaluation of noise in the UL scenario are presented in Section II. The optical wireless channel and the characteristics of random device orientation and link blockage are introduced in Section III as a preliminary of Section IV. The analytical results of the optical wireless channel statistics and the SNR statistics are presented in Section IV. In Section V, evaluation of the UL transmission coverage probability is presented. Finally, conclusions are drawn in Section VI.

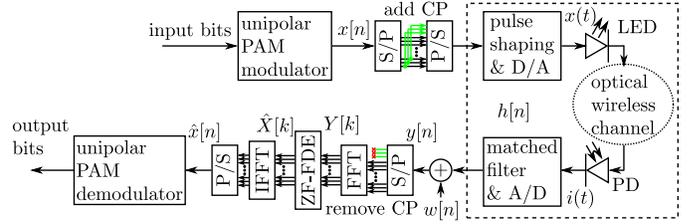


Figure 1: Block diagram of the optical wireless UL transmission based on PAM-SCFDE.

II. WIRELESS INFRARED-BASED TRANSMISSION IN THE UPLINK SCENARIO

A. Uplink transmission system model with PAM-SCFDE

PAM-SCFDE transmission has a low PAPR and a low computational complexity on the transmitter side (UE) [22], which is consistent with the nature of UL transmission [14]. Therefore, we consider a wireless IR transmission using PAM-SCFDE in this study as an example. The block diagram of a PAM-SCFDE-based OWC system is shown in Fig. 1. Firstly, the information bits are modulated using unipolar pulse amplitude modulation (PAM) symbols which can be defined as:

$$x[n] = \bar{p}\beta m_n, \quad (1)$$

where \bar{p} is the LED optical power, m_n takes the integer values of $m_n \in \{0, 1, \dots, M-1\}$ and β is a scaling factor to make the signal average optical power matches the LED optical power $\mathbb{E}_n\{x[n]\} = \bar{p}$. This leads to $\beta = 1/\mathbb{E}_n\{m_n\} = \frac{2}{M-1}$ where $\mathbb{E}\{\cdot\}$ is the statistical expectation. After the addition of a cyclic prefix (CP), the discrete PAM signal $x[n]$ is forwarded to a channel with a discrete-time impulse response of $h[n]$. The channel is composed of a series of processes including pulse shaping with digital-to-analogue (D/A) conversion, electrical-to-optical (E/O) conversion via LED, transmission over an optical wireless channel, optical-to-electrical (D/A) conversion via PD and matched filtering with analogue-to-digital (A/D) conversion. The signal after pulse shaping can be written as:

$$x(t) = \sum_{n=-\infty}^{\infty} x[n]h_{sp}(t - nT_s), \quad (2)$$

where $h_{sp}(t)$ is the impulse response of the signal pulse function and T_s is the symbol period. The LED, optical wireless channel and PD counterparts have low pass characteristics and have various responses on different wavelength λ . Therefore, the output photocurrent of the PD can be calculated as:

$$i(t) = \mathcal{M} \int_{\lambda_{\min}}^{\lambda_{\max}} \mathcal{G}_{of}(\lambda) h_{pd}(t, \lambda) * h_{ow}(t, \lambda) * h_{led}(t, \lambda) * x(t) d\lambda, \quad (3)$$

where $(*)$ refers to the convolution operator; \mathcal{M} is the average avalanche photodiode (APD) gain; $\mathcal{G}_{of}(\lambda)$ is the optical filter spectrum transmittance; $h_{led}(t, \lambda)$, $h_{ow}(t, \lambda)$ and $h_{pd}(t, \lambda)$ are the wavelength-dependent impulse responses of LED, optical wireless channel and PD, respectively. Without loss of generality, the cases with both positive-intrinsic-negative (PIN) diodes and with APDs are considered here. In the case with a PIN

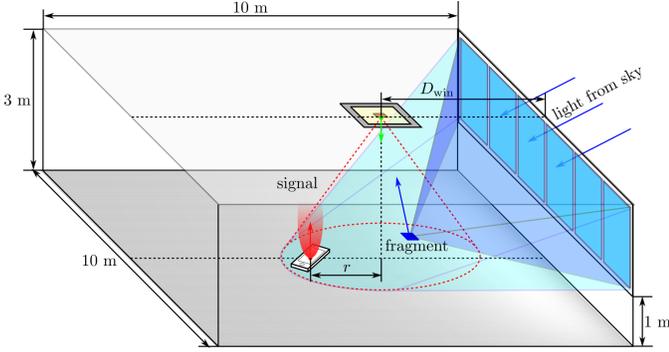


Figure 2: The geometry of simulating the shot noise photocurrent.

diode, the APD gain equals unity ($\mathcal{M} = 1$); the integration limits λ_{\min} and λ_{\max} are determined by the spectrum range of the LED. Finally, the photocurrent is forwarded to a matched filter and sampled at nT_s to obtain the received discrete samples. By applying a discrete-time unit impulse function input $x[n] = \delta[n]$ to (2) and inserting (2) into (3), the continuous-time impulse response after convolving with the signal pulse $h_{\text{sp}}(t)$ but before the matched filter sampling at nT_s can be written as:

$$\begin{aligned} h(t) &= \{i * h_{\text{sp}}\}(t)|_{x[n]=\delta[n]} \\ &= \mathcal{M} \int_{\lambda_{\min}}^{\lambda_{\max}} \mathcal{G}_{\text{of}}(\lambda) \{h_{\text{sp}} * h_{\text{pd}} * h_{\text{ow}} * h_{\text{led}} * h_{\text{sp}}\}(t, \lambda) d\lambda. \end{aligned} \quad (4)$$

By sampling at nT_s , the equivalent discrete-time channel $h[n] = h(nT_s)$ can be obtained. Then, the received discrete-time samples can be represented by:

$$y[n] = h[n] * x[n] + w[n], \quad (5)$$

where $w[n]$ is the noise sample after the matched filter. Next, CPs are removed and received samples are grouped by blocks of K samples, which is followed by the frequency domain equalisation. The frequency-domain samples $Y[k]$ can be calculated using the fast Fourier transform (FFT) of $y[n]$ as:

$$Y[k] = \mathcal{F}_{\text{ft}}\{y[n]\} = H[k]X[k] + W[k], \quad (6)$$

where $H[k]$, $X[k]$ and $W[k]$ are the FFT of $h[n]$, $x[n]$ and $w[n]$, respectively. By applying the single-tap equalisation with the zero-forcing criterion, the recovered frequency domain symbols can be written as:

$$\hat{X}[k] = \frac{Y[k]}{H[k]} = X[k] + \frac{W[k]}{H[k]}. \quad (7)$$

Finally, the time-domain symbols are obtained using the inverse fast Fourier transform (IFFT). With appropriate scaling and PAM decoding, the transmission is completed. According to (1), the electrical power of signal can be calculated as: $P_{\text{elec}} = \mathbb{E}_n \{x^2[n]\} = \bar{p}^2 \beta^2 \mathbb{E}_n \{\mathbf{m}_n^2\} = \frac{2\bar{p}^2(2M-1)}{3(M-1)}$. With a double-sided noise power spectral density (PSD) of N_0 , the

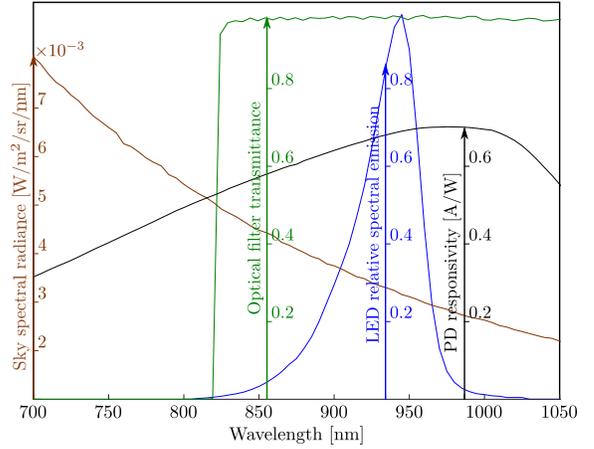


Figure 3: Wavelength dependent parameters. Optical source: Vishay VSMY3940X01-GS08 infrared emitter, detector: Hamamatsu S11519-30 Si APD, optical filter: Shamerock BLP01-808R-25 long-pass filter. The background spectral radiance is extracted from the curve D in Fig. 4 of [27].

noise variance after zero-forcing equalisation can be calculated by [23]:

$$\sigma_w^2 = \sum_{k=0}^{K-1} \mathbb{E}_n \left\{ \left| \frac{W[k]}{H[k]} \right|^2 \right\} \frac{1}{KT_s} = \frac{N_0}{KT_s} \sum_{k=0}^{K-1} \frac{1}{|H[k]|^2}. \quad (8)$$

Thus, the SNR calculation can be concluded as:

$$\gamma = \frac{P_{\text{elec}}}{\sigma_w^2} = \frac{2\bar{p}^2(2M-1)KT_s}{3(M-1)N_0 \sum_{k=0}^{K-1} |H[k]|^{-2}}. \quad (9)$$

Next, we consider the calculation of $H[k]$. By applying Fourier transform to (4), the corresponding continuous-time channel frequency response can be obtained as:

$$\begin{aligned} H(f) &= \mathcal{F}\{h(t)\} = \mathcal{M} \int_{\lambda_{\min}}^{\lambda_{\max}} \mathcal{G}_{\text{of}}(\lambda) \\ &\quad \times H_{\text{sp}}^2(f) H_{\text{pd}}(f, \lambda) H_{\text{ow}}(f, \lambda) H_{\text{led}}(f, \lambda) d\lambda, \end{aligned} \quad (10)$$

where $H_{\text{sp}}(f)$, $H_{\text{pd}}(f, \lambda)$, $H_{\text{ow}}(f, \lambda)$ and $H_{\text{led}}(f, \lambda)$ are the Fourier transform of $h_{\text{sp}}(t)$, $h_{\text{pd}}(t, \lambda)$, $h_{\text{ow}}(t, \lambda)$ and $h_{\text{led}}(t, \lambda)$, respectively. According to the sampling theorem and Poisson summation formula, the frequency response of the discrete-time channel can be obtained from a periodic summation of the continuous-time channel frequency response as: $H_s(f) = \sum_{l=-\infty}^{\infty} H\left(f - \frac{l}{T_s}\right)$. According to the relationship between discrete Fourier transform (DFT) and discrete-time Fourier transform (DTFT), the values of $H[k]$ are equal to the values of $H_s(f)$ at frequencies $f = \frac{k}{KT_s}$ for $k = 0, 1, \dots, K-1$ [24]:

$$H[k] = H_s\left(\frac{k}{KT_s}\right) = \sum_{l=-\infty}^{\infty} H\left(\frac{k}{KT_s} - \frac{l}{T_s}\right). \quad (11)$$

Despite the limits of the summation in (11) from $-\infty$ to ∞ , the signal pulse $H_{\text{sp}}(f)$ is generally bandlimited, which makes the $H\left(\frac{k}{KT_s} - \frac{l}{T_s}\right) = 0$ for $k = 0, 1, \dots, K-1$ with $l \in (-\infty, -1] \cup [2, \infty)$. In this study, the root-square raised cosine (RRC) function is used as the signal pulse. Regarding

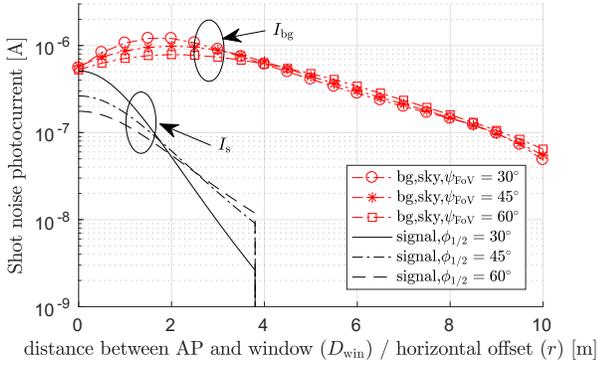


Figure 4: Background shot noise photocurrent against the distance between AP and the windows D_{win} . Signal dependent shot noise photocurrent against the horizontal offset r with a detector field of view (FoV) of 60° .

Table I: Simulation parameters I

Parameter	Symbol	Value
LED optical power	\bar{p}	200 mW
PD physical area	A_{pd}	7.1 mm ²
excessive noise index	ξ	0.3
concentrator refractive index	n	1.5
absolute temperature	\mathcal{T}_a	300 K
load resistance	R_L	50 Ω
reflectivity [floor/walls/ceiling]	$\rho_f/\rho_w/\rho_c$	0.3/0.8/0.8
AP height/UE height	z_a/z_u	3/0.75 m

the frequency and wavelength dependent characteristics of the LED and the PD, the following functions are used [25], [26]:

$$H_{\text{led}}(f, \lambda) = \frac{S_{\text{led}}(\lambda)}{1 + \frac{jf}{f_{c,\text{led}}}}, H_{\text{pd}}(f, \lambda) = \frac{\mathcal{R}_{\text{pd}}(\lambda)}{1 + j2\pi C_T R_L f}, \quad (12)$$

where $f_{c,\text{led}}$ is the LED cut-off frequency; $S_{\text{led}}(\lambda)$ is the normalised spectral intensity of the LED which has $\int_{\lambda_{\text{min}}}^{\lambda_{\text{max}}} S_{\text{led}}(\lambda) d\lambda = 1$; C_T is the PD terminal capacitance; R_L is the load resistance and $\mathcal{R}_{\text{pd}}(\lambda)$ is the PD spectral responsivity without APD gain.

B. Receiver noise in the uplink scenario

In an OWC system, the receiver noise is primarily composed of a thermal noise and a shot noise. In the LiFi UL scenario, the receiver PD is mounted on the ceiling and directed towards the floor. In this scenario, the background light directly radiated from the sky entering the window is unlikely to be detected by the ceiling-mounted PD with a limited FoV, but propagates to the detector via reflections (primarily by the floor). Consequently, the level of background shot noise might be lower than the case in a DL VLC system. In addition, an optical power of 100 to 500 mW is typically used for a wide beam IR emitter [28]. In contrast, the optical power of visible light luminaries is in the range from a few to tens of Watts. This implies that the level of signal-dependent shot noise might also be lower in the UL scenario. Therefore, we simulate the noise PSD of background, signal-dependent shot noise and the thermal noise in a typical UL scenario in order to find out which of them is the dominant source of receiver noise.

The simulation environment is conducted in a room of size 10 m \times 10 m \times 3 m, as shown in Fig. 2. The windows are on

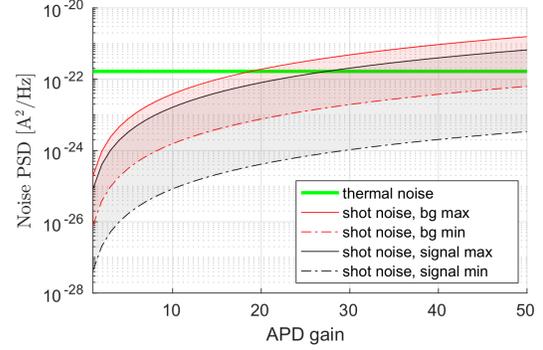


Figure 5: Receiver noise PSD against APD gain. The regions of shot noise PSD correspond to the highest/lowest values shown in Fig. 4.

the right hand side of the room. The top and bottom edges of the windows are 3 m and 1 m above the floor, respectively. The remaining simulation parameters are listed in Table I and the wavelength dependent parameters are depicted in Fig. 3. Note that a LED optical power of 200 mW is lower than the maximum exposure limit for eye safety concerns according to the standard for Photobiological safety of lamp and lamp systems [29]. The floor area is divided into small square fragments. The solid angle with respect to the windows and the centre of each square fragment is calculated. In conjunction with the sky spectral radiance, the incident optical power on each floor fragment is calculated. A LiFi AP is deployed on the horizontal mid-line of the room and is D_{win} away from the window, as shown in Fig. 2. The limited FoV makes the UL detector receive light only from a confined circular region on the floor centred at the AP location. With an increase to the distance D_{win} , the circular region shift to the left, and the corresponding amount of background light entering the detector also changes. Thus, the background photocurrent I_{bg} is evaluated with various values of D_{win} , and the results with detector FoV values of 30° , 45° and 60° are presented in Fig. 4. The range of I_{bg} is between 5×10^{-8} and 1.2×10^{-6} A. It reaches its maximum when D_{win} is about 2 m and starts to decrease with further increases in D_{win} . Regarding the signal dependent shot noise, we consider a UL LED facing upward towards the ceiling with a horizontal offset to the PD of r , as demonstrated in Fig. 2. For each horizontal offset r , the signal photocurrent I_s is evaluated and the results are also presented in Fig. 4. The range of I_s is between 2.6×10^{-9} and 5.1×10^{-7} A. Intuitively, the value of I_s decreases with an increase of r and the rate is higher with a smaller half-power semiangle $\phi_{1/2}$. It is assumed that the light from DL light sources causes no interference due to the use of different optical spectra. Finally, we evaluate the PSD of each noise source. The noise PSD can be calculated by the summation of the thermal noise PSD N_0^{th} and the shot noise PSD N_0^{sh} as [26]:

$$N_0 = N_0^{\text{th}} + N_0^{\text{sh}}, \quad \text{with } N_0^{\text{th}} = \frac{2\mathcal{K}_b \mathcal{T}_a}{R_L}$$

$$\text{and } N_0^{\text{sh}} = q\mathcal{M}^{2+\xi}(I_{\text{bg}} + I_s), \quad (13)$$

where \mathcal{K}_b is the Boltzmann's constant, \mathcal{T}_a is the absolute

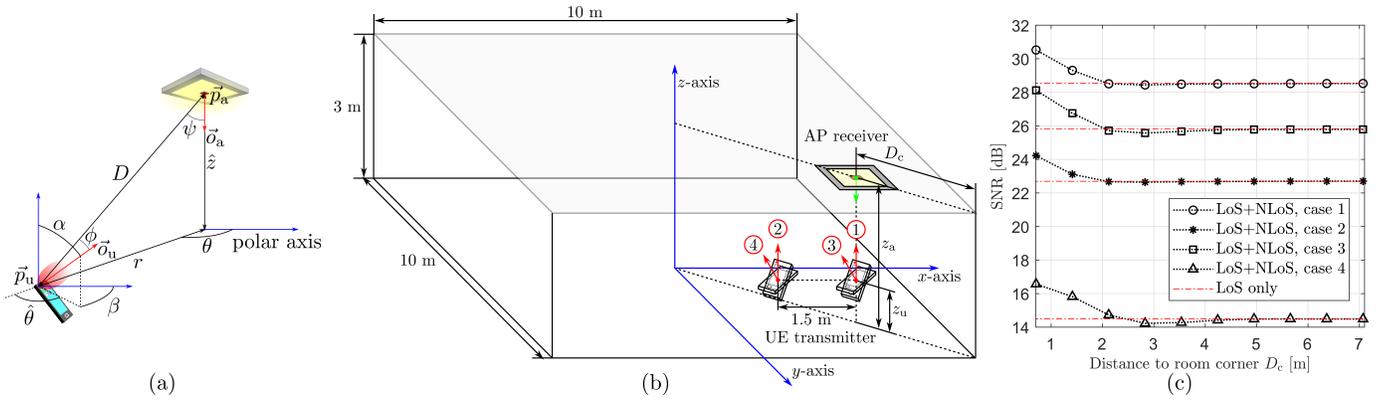


Figure 6: (a) The LiFi UL geometry. (b) Geometry of simulation with non-line-of-sight (NLoS) channel. Case 1: aligned; case 2: shifted; case 3: tilted; case 4: shifted and tilted. (c) SNR against the distance from AP to room corner D_c .

temperature, q is the electric charge and χ is the excessive noise index. The result of noise PSD against APD gain \mathcal{M} is presented in Fig. 5. In the case of using a PIN diode ($\mathcal{M} = 1$), the thermal noise PSD (1.7×10^{-22} A²/Hz) is significantly higher than the shot noise PSD ($< 2 \times 10^{-25}$ A²/Hz). In the case where an APD is used, the shot noise PSD will increase to roughly the same level of thermal noise with $\mathcal{M} = 50$, as shown in Fig. 5. With a further increase of \mathcal{M} , shot noise starts to be dominant noise source.

III. OPTICAL WIRELESS CHANNEL WITH RANDOM ORIENTATION AND LINK BLOCKAGE

In this section, we focus on introducing the characteristics of the optical wireless channel including the properties of random device orientation and link blockage as a preliminary for the next section. The UL geometry is illustrated in Fig. 6 (a), where the UL signal is emitted from a LED mounted on the front of a UE and detected by a PD installed on a LiFi AP located on the ceiling. The optical wireless channel is composed of line-of-sight (LoS) and NLoS components, which can be described by: $H_{ow}(f, \lambda) = G + H_{nlos}(f, \lambda)$, where G is the LoS component directly from the LED to the PD; $H_{nlos}(f, \lambda)$ is the NLoS components due to indoor internal surface reflections.

A. Line-of-sight channel

The LoS channel can be characterised by [30]:

$$G = \frac{(m+1)A_{pd}g_c g_v}{2\pi D^2} \cos^m \phi \cos \psi, \quad (14)$$

where D is the Euclidean norm between the LED and the PD, ϕ and ψ are the corresponding radiant/incident angles, A_{pd} denotes the active area of the PD, g_c denotes an optical concentrator gain, g_v is a visibility factor and m is the Lambertian mode number which is related to the LED half-power semiangle $\phi_{1/2}$ by $m = -1/\log_2(\cos \phi_{1/2})$. The value of the concentrator gain is calculated by $g_c = n^2/\sin^2 \psi_{FoV}$, where n is the refractive index of the concentrator material and ψ_{FoV} is the FoV of the PD. The visibility factor g_v equals zero when one or more of the following three conditions are true: a) $\phi > \pi/2$, b) $\psi > \psi_{FoV}$, c) there is a link blockage.

Now, we consider a three-dimensional Cartesian coordinate system x - y - z with the origin right below the AP at the floor level, as shown in Fig. 6 (a). The PD position and orientation are defined as $\vec{p}_a = (0, 0, z_a)$ and $\vec{o}_a = (0, 0, -1)$, where z_a is the height of the AP above the floor. If the horizontal offset between the UE and AP is r , the position of the LED can be defined as $\vec{p}_u = (r \cos \theta, r \sin \theta, z_u)$, where z_u is the height of the UE above the floor and θ is the azimuth angle of the UE position relative to the x -axis. Defining the UE orientation with an elevation angle of α and an azimuth angle of β , the corresponding Cartesian coordinate becomes $\vec{o}_u = (\cos \beta \sin \alpha, \sin \beta \sin \alpha, \cos \alpha)$. The quantities D , $\cos \phi$, and $\cos \psi$ in (14) can be rewritten as functions of \vec{p}_a , \vec{o}_a , \vec{p}_u and \vec{o}_u as: $D = \|\vec{p}_u - \vec{p}_a\| = \sqrt{r^2 + \hat{z}^2}$, $\cos \phi = \frac{\vec{o}_u \cdot \{\vec{p}_a - \vec{p}_u\}^T}{D} = \frac{\hat{z} \cos \alpha - r \sin \alpha \cos \hat{\theta}}{\sqrt{r^2 + \hat{z}^2}}$ and $\cos \psi = \frac{\vec{o}_a \cdot \{\vec{p}_u - \vec{p}_a\}^T}{D} = \frac{\hat{z}}{\sqrt{r^2 + \hat{z}^2}}$ [31], where $\{\cdot\}^T$ is the transpose of a vector or matrix, (\cdot) is the dot product operator, $\hat{z} = z_a - z_u$ and $\hat{\theta} = \theta - \beta$. By using these equations, expression (14) can be rewritten as:

$$G = \frac{(m+1)A_{pd}g_c g_v}{2\pi (r^2 + \hat{z}^2)^{\frac{m+3}{2}}} \left(\hat{z} \cos \alpha - r \sin \alpha \cos \hat{\theta} \right)^m. \quad (15)$$

B. Non-line-of-sight channel

The NLoS channel is another part of the optical wireless channel, which is caused by the reflection of internal surfaces in the room. Here we use simulations in a number of typical scenarios to evaluate the significance of NLoS channels. The frequency-domain method presented in [32] has been selected to construct the NLoS channel, because this simulation tool has a lower complexity and it directly provides results in terms of the channel frequency response $H_{ow}(f, \lambda)$. The simulation is conducted in a room of size 10 m \times 10 m \times 3 m, as shown in Fig. 6 (b). An AP is deployed on the diagonal on the ceiling with the PD facing the floor. The AP is D_c away from one of the corners of the room. A half-power semiangle of $\phi_{1/2} = 60^\circ$ and an APD gain of $\mathcal{M} = 50$ are used. The remaining simulation parameters are the same as those listed in Table I and those depicted in Fig. 3. To ensure the simulation covers various user conditions (aligned/shifted/tilted), four user cases are considered, as illustrated in Fig. 6 (b). The LED faces upwards ($\vec{o}_u = (0, 0, 1)$) in case 1 and 2, and is

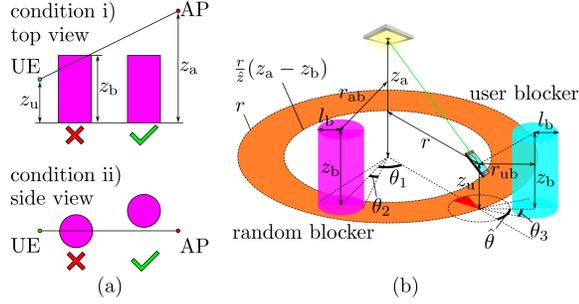


Figure 7: (a) Necessary conditions of link blockage. (b) Geometry of RB and UB.

tilted with an orientation of $\vec{d}_u = (0.5, 0.5, 0.7071)$ in case 3 and 4. On the other hand, the UE is right below the AP in case 1 and 3, and is shifted in the direction of $-x$ by 1.5 m in case 2 and 4. The results of the SNR against D_c with and without a NLoS channel are presented in Fig. 6 (c). It can be observed that there is a perceivable difference between the SNR results with and without a NLoS channel of up to about 2 dB when $D_c \leq 2$ m. The SNR difference decreases with the increase of D_c and becomes negligible when D_c is greater than 2 m. This implies that the LiFi UL performance is barely affected by the NLoS channel when the wireless link is located far from the edges of the room and the overall channel frequency response is dominated by characteristics of the frontends and signal pulses. The calculation of the NLoS channel has high complexity and is challenging to analyse. Therefore, we omit the NLoS channel in the following analysis for simplicity ($H_{ow}(f, \lambda) = G$) and treat the analysis of links next to the room edge as a special case that are reserved for future study.

C. Random orientation

Due to the characteristics of user behaviour, the UE orientation related angles α and β in (15) become random variables, as shown in Fig. 6 (a). An experimental study on the statistics of α and β are presented in [33]. The authors approximate the statistic of α by a Laplace distribution for static sitting users. The corresponding probability density function (PDF) is concluded as:

$$f_\alpha(\alpha) = \frac{1}{2b_L} \exp\left(-\frac{|\alpha - \mu_L|}{b_L}\right) \text{ for } \alpha \in [0, \pi/2] \quad (16)$$

where $\mu_L = 41.06^\circ$ is the average elevation angle and $b_L = \sqrt{\sigma_L^2}/2$ with $\sigma_L = 7.30^\circ$. The value of μ_L and σ_L was estimated in the experiment carried out in [33]. The angle β follows a uniform distribution as there is no bias on the direction of a user. Since β is a deterministic angle for a static user, the angle $\hat{\theta} = \theta - \beta$ also follows a uniform distribution. The PDF of $\hat{\theta}$ can be written as:

$$f_{\hat{\theta}}(\hat{\theta}) = \frac{1}{2\pi} \text{ for } \hat{\theta} \in [-\pi, \pi]. \quad (17)$$

D. Link blockage

Regarding the link blockage events, we use a cylindrical object with a height of z_b and a radius of l_b to model the human blocker [34], as shown in Fig. 7. There are two necessary

conditions for determining whether a blocker is obstructing a specific LoS path with given UE and AP positions [34]:

- i) From the side view, the blocker is high enough to have the possibility to come into contact the LoS segment;
- ii) From the top view, the LoS segment intersects with the blocker circle,

as illustrated in Fig. 7 (a). In this study, two categories of human blockers are considered. The first category is defined as a random blocker (RB), which considers the nearby random people in the room. The second category is defined as a user blocker (UB), which considers the user of the device who is always next to the UE. The geometry of the two types of blockers are also shown in Fig. 7 (b).

1) *Random blocker*: As shown in Fig. 7 (b), the horizontal separation between the RB and the AP is defined as r_{ab} . If $r_{ab} \in [r \frac{z_a - z_b}{z}, r]$, the blocking condition i) is fulfilled [34]. If $|\theta_1| \leq \theta_2 = \arcsin(l_b/r_{ab})$, the blocking condition ii) is fulfilled. Assuming that there are N_b RBs randomly distributed in a circular area centred at the AP with a radius of r_{ab} , the average blockage probability for a UE that is r away from the AP is concluded as [34]:

$$\hat{\mathcal{P}}_b(N_b, r_{ab}) = 1 - \left(1 - \frac{2l_b r (z_b - z_u)}{\pi r_{ab}^2 z}\right)^{N_b}. \quad (18)$$

If the two-dimensional spatial position of the RBs follows a homogeneous Poisson point process (PPP) with a density of Λ_b , the number of involved RB N_b follows a Poisson distribution with a mean of $\Lambda_b \pi r^2$. Therefore, the average blockage probability caused by RBs for a UE that is r away from the AP can be derived as:

$$\begin{aligned} \mathcal{P}_{rb} = 1 - \mathcal{P}_{los} &= \sum_{N_b=0}^{\infty} \hat{\mathcal{P}}_b(N_b, r) \frac{(\Lambda_b \pi r^2)^{N_b} e^{-\Lambda_b \pi r^2}}{N_b!} \\ &= 1 - \exp\left(-2l_b r \Lambda_b \frac{z_b - z_u}{z}\right), \end{aligned} \quad (19)$$

where \mathcal{P}_{los} represents the probability that the LoS path is clear.

2) *User blocker*: On the other hand, the UB is correlated with the status of the UE position and orientation. Firstly, the UB is always next to the UE. Therefore, a fixed separation of r_{ub} between the UB and UE is defined, as illustrated in Fig. 7 (b). If $r \geq \frac{z}{z_b - z_u} r_{ub}$, the blocking condition i) is fulfilled [35]. In most of the practical scenarios, the front side of the UE is always facing the user. This means that the UB position is determined by $\hat{\theta}$. The blocking condition ii) is fulfilled when $|\hat{\theta}| \geq \pi - \theta_3$ as illustrated in Fig. 7 (b), where $\theta_3 = \arcsin(l_b/r_{ub})$. Since the occurrence of blockage caused by the UB is correlated with the random angle β , their effects on the statistics of the optical wireless channel will be considered in Section IV.

IV. STATISTICS OF OPTICAL WIRELESS CHANNEL AND SNR

In this section, we consider the cumulative distribution function (CDF) of the optical wireless channel and the CDF of the SNR in the UL scenario based on the models, characteristics of link blockage and random device orientation introduced in

$$F_G(T) = \begin{cases} \mathcal{P}_{\text{rb}} + \mathcal{P}_{\text{los}} \left(\frac{1_S \theta_3}{\pi} \mathcal{C}_{0,\alpha_1} + \mathcal{C}_{\alpha_1, \frac{\pi}{2}} + \mathcal{A}_{\alpha_3, \alpha_6}^{a_3, b_3} + \mathcal{A}_{\alpha_6, \alpha_4}^{a_2, b_2} + \mathcal{A}_{\alpha_4, \alpha_1}^{a_1, b_1} \right) & : T \in (0, T_1] \\ \mathcal{P}_{\text{rb}} + \mathcal{P}_{\text{los}} \left(\frac{1_S \theta_3}{\pi} \mathcal{C}_{\alpha_2, \alpha_1} + \mathcal{C}_{0, \alpha_2} + \mathcal{C}_{\alpha_1, \frac{\pi}{2}} + \mathcal{A}_{\alpha_2, \alpha_5}^{a_1, b_1} + \mathcal{A}_{\alpha_5, \alpha_4}^{a_2, b_2} + \mathcal{A}_{\alpha_4, \alpha_1}^{a_1, b_1} \right) & : T \in (T_1, T_2] \\ \mathcal{P}_{\text{rb}} + \mathcal{P}_{\text{los}} \left(\frac{1_S \theta_3}{\pi} \mathcal{C}_{\alpha_2, \alpha_1} + \mathcal{C}_{0, \alpha_2} + \mathcal{C}_{\alpha_1, \frac{\pi}{2}} + \mathcal{A}_{\alpha_2, \alpha_1}^{a_1, b_1} \right) & : T \in (T_2, T_3] \end{cases}, \quad (20)$$

where

$$\mathcal{A}_{u,v}^{a,b} = \frac{b}{\pi} \mathcal{C}_{u,v} - \frac{a \varkappa T^{\frac{1}{m}}}{r b_L \pi} \left(\left\{ \mathcal{B}_{(\mu_L \wedge u), v}^{1, -1} \right\}^+ + \left\{ \mathcal{B}_{u, (\mu_L \vee v)}^{1, +1} \right\}^+ \right) + \frac{a \hat{z}}{2 r b_L \pi} \left(\left\{ \mathcal{B}_{(\mu_L \wedge u), v}^{2, -1} + \mathcal{B}_{(\mu_L \wedge u), v}^{0, -1} \right\}^+ + \left\{ \mathcal{B}_{u, (\mu_L \vee v)}^{2, +1} + \mathcal{B}_{u, (\mu_L \vee v)}^{0, +1} \right\}^+ \right), \quad \text{with } \varkappa = \left(\frac{2\pi (r^2 + \hat{z}^2)^{\frac{m+3}{2}}}{\hat{z} A_{\text{Pd}} (m+1) \mathbf{g}_c} \right)^{1/m}, \quad (21)$$

$$\mathcal{B}_{u,v}^{\kappa, s} = \frac{{}_2F_1 \left(1, \frac{\kappa}{2} - \frac{s_j}{2b_L}; 1 + \frac{\kappa}{2} - \frac{s_j}{2b_L}; e^{2uj} \right) - {}_2F_1 \left(1, \frac{\kappa}{2} - \frac{s_j}{2b_L}; 1 + \frac{\kappa}{2} - \frac{s_j}{2b_L}; e^{2vj} \right)}{\left(\kappa - \frac{s_j}{b_L} \right) e^{-u \left(\kappa j + \frac{s}{b_L} \right) + \frac{s \mu_L}{b_L}} - \left(\kappa - \frac{s_j}{b_L} \right) e^{-v \left(\kappa j + \frac{s}{b_L} \right) + \frac{s \mu_L}{b_L}}}, \quad (22)$$

$$\mathcal{C}_{u,v} = \frac{1}{2} \left(e^{\frac{\{v-\mu_L\}^-}{b_L}} - e^{\frac{\{u-\mu_L\}^-}{b_L}} - e^{-\frac{\{v-\mu_L\}^+}{b_L}} + e^{-\frac{\{u-\mu_L\}^+}{b_L}} \right), \quad (23)$$

$$\alpha_1 = \mathcal{D}_{+1}^{+1} \left(\frac{1_S l_b^2}{r_{\text{ub}}^2} \right), \alpha_2 = \mathcal{D}_{-1}^{+1} \left(\frac{1_S l_b^2}{r_{\text{ub}}^2} \right), \alpha_3 = \mathcal{D}_{+1}^{-1} (0), \alpha_4 = \mathcal{D}_{+1}^{+1} (1 - u_t^2), \alpha_5 = \mathcal{D}_{-1}^{+1} (1 - u_t^2), \alpha_6 = \mathcal{D}_{+1}^{-1} (1 - u_t^2), \quad (24)$$

$$\mathcal{D}_{s_2}^{s_1}(u) = \frac{\pi}{2} \vee \left(s_1 \arctan \left(\frac{r}{\hat{z}} \sqrt{1-u} \right) + s_2 \arccos^\dagger \left(\varkappa T^{1/m} / \sqrt{r^2(1-u) + \hat{z}^2} \right) \right), \quad (25)$$

$$T_1 = (\hat{z}/\varkappa)^m, T_2 = \left(\sqrt{u_t^2 r^2 + \hat{z}^2} / \varkappa \right)^m, T_3 = \left(\sqrt{(1 - 1_S l_b^2 / r_{\text{ub}}^2) r^2 + \hat{z}^2} / \varkappa \right)^m. \quad (26)$$

Table II: Coefficient and threshold of linear functions

a_1	a_2	a_3	b_1	b_2	b_3	u_t
-1.997	-1.0496	-1.997	0.9262	1.5708	2.2154	0.65

Section III. The analytical results with expressions in closed-form are concluded in the following proposition and corollary.

A. Statistics of optical wireless channel

Proposition 1. *Provided the system parameters r , z_a , z_u , z_b , m , A_{Pd} , ψ_{FoV} , \mathbf{n} , Λ_b , l_b and r_{ub} (defined in Section III), the CDF of the optical wireless channel G can be calculated by (20). Note that $\hat{z} = z_a - z_u$, $\theta_3 = \arcsin(l_b/r_{\text{ub}})$ and 1_S is an indicator function, which equals one if the condition $\mathcal{S} = \{r|r \geq \hat{z} r_{\text{ub}} / (z_b - z_u)\}$ is fulfilled and equals zero otherwise. The values of μ_L , b_L , \mathcal{P}_{rb} and \mathcal{P}_{los} are as specified in (16) and (19), respectively. The values a_1 , a_2 , a_3 , b_1 , b_2 , b_3 and u_t are listed in Table II. In addition, the following operators are used: $\{u\}^+ = \max(u, 0)$, $\{u\}^- = \min(u, 0)$, $u \vee v = \min(u, v)$ and $u \wedge v = \max(u, v)$. In (22) and (25), the inputs s , s_1 and s_2 can only equals to ± 1 to control the sign of terms. The function $\arccos^\dagger(u)$ is a variant of the conventional inverse trigonometric function $\arccos(u)$ with an extended variable domain of $(-\infty, \infty)$. In the extended variable domain, $\arccos^\dagger(u) = \pi$ for $u < -1$ and $\arccos^\dagger(u) = 0$ for $u > 1$. The function ${}_2F_1(u_1, u_2; u_3; u_4)$ is the hypergeometric function. In the case that the optical wireless channel threshold is greater than the maximum possible value ($T > T_3$) or the UE is outside the FoV of the UL detector ($r > \hat{z} \tan \psi_{\text{FoV}}$), the channel CDF becomes $F_G(T) = 1$.*

Proof: Firstly, we consider the conditional probability $\mathbb{P}[G \leq T|\alpha]$ without link blockage caused by RBs. By applying the expression (15) to the inequality $G \leq T$, the set of $\hat{\theta}$ that fulfils the condition can be found as: $\Theta_1 = \left\{ \hat{\theta} : |\hat{\theta}| \leq \arccos^\dagger(\xi) \right\}$, where

$$\xi = \frac{\hat{z} \cos \alpha - \varkappa T^{\frac{1}{m}}}{r \sin \alpha}. \quad (28)$$

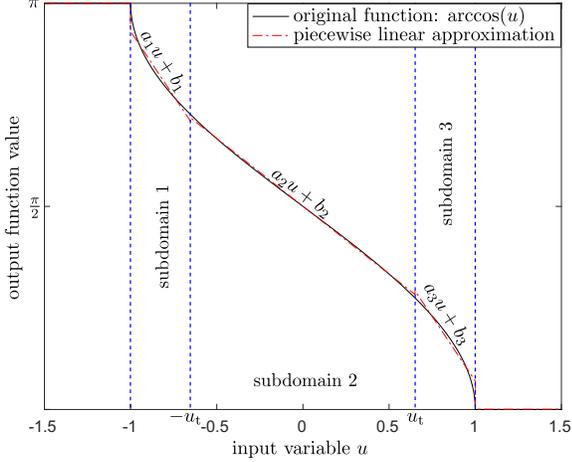
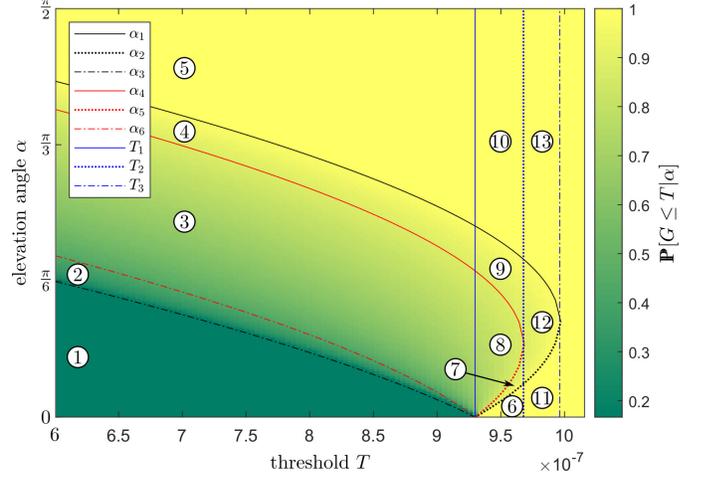
Note that \varkappa is specified in (21), and $\mathbf{g}_v = 1$ is used here, because all cases with $\mathbf{g}_v = 0$ are treated individually in the following derivation. In addition, the condition $G \leq T$ is also fulfilled if link blockage caused by the UB occurs. Therefore, another set of $\hat{\theta}$ that leads to $G \leq T$ can be found based on the discussion in Section III-D2: $\Theta_2 = \left\{ \hat{\theta} : |\hat{\theta}| \geq \pi - 1_S \theta_3 \right\}$. Note that if the UE is too close to the AP, the blocking condition i) does not hold. Therefore, the indicator function 1_S equals zero and Θ_2 will be \emptyset as $\hat{\theta} \in [-\pi, \pi)$. Combining the two cases and in conjunction to the distribution of $\hat{\theta}$ (17), we can calculate the conditional probability as:

$$\begin{aligned} \mathbb{P}[G \leq T|\alpha] &= \int_{\Theta_1 \cup \Theta_2} f_{\hat{\theta}}(\hat{\theta}) d\hat{\theta} \\ &= \min \left(\frac{1}{\pi} \arccos^\dagger(\xi) + \frac{1_S \theta_3}{\pi}, 1 \right). \end{aligned} \quad (29)$$

In order to obtain the final CDF, the calculation of the following integral will be required:

$$\begin{aligned} &\int_u^v f_{\alpha}(\alpha) \frac{\arccos^\dagger(\xi)}{\pi} d\alpha \\ &= \int_u^v \frac{e^{-\frac{|\alpha - \mu_L|}{b_L}}}{2b_L \pi} \arccos^\dagger \left(\frac{\hat{z} \cos \alpha - \varkappa T^{\frac{1}{m}}}{r \sin \alpha} \right) d\alpha, \end{aligned} \quad (30)$$

$$\begin{aligned} \mathcal{A}_{u,v}^{a,b} &= \int_u^v \frac{e^{-\frac{|\alpha-\mu_L|}{b_L}}}{2b_L\pi} \left(a \frac{\hat{z} \cos \alpha - \varkappa T^{\frac{1}{m}}}{r \sin \alpha} + b \right) d\alpha = \frac{b}{\pi} \int_u^v \frac{e^{-\frac{|\alpha-\mu_L|}{b_L}}}{2b_L} d\alpha - \frac{a\varkappa T^{\frac{1}{m}}}{2rb_L\pi} \left(\left\{ \int_u^{\min(\mu_L,v)} \frac{e^{-\frac{\alpha-\mu_L}{b_L}}}{\sin \alpha} d\alpha \right\}^+ \right. \\ &+ \left. \left\{ \int_{\max(\mu_L,u)}^v \frac{e^{-\frac{\alpha-\mu_L}{b_L}}}{\sin \alpha} d\alpha \right\}^+ \right) + \frac{a\hat{z}}{2rb_L\pi} \left(\left\{ \int_u^{\min(\mu_L,v)} \frac{e^{-\frac{\alpha-\mu_L}{b_L}}}{\tan \alpha} d\alpha \right\}^+ + \left\{ \int_{\max(\mu_L,u)}^v \frac{e^{-\frac{\alpha-\mu_L}{b_L}}}{\tan \alpha} d\alpha \right\}^+ \right). \end{aligned} \quad (27)$$


 Figure 8: Approximation of $\arccos^\dagger(u)$ using a piecewise linear function.

 Figure 9: Illustration of the breakpoints of the function $\mathbb{P}[G \leq T|\alpha]$, which corresponds to Table III.

which is challenging to solve. In order to increase the calculation tractability of (30), we attempt to use the following piecewise linear function to approximate the function $\arccos^\dagger(u)$:

$$\arccos_{\text{apx}}^\dagger(u) = \begin{cases} a_1 u + b_1 : & -1 < u < -u_t \\ a_2 u + b_2 : & -u_t \leq u \leq u_t \\ a_3 u + b_3 : & u_t < u < 1 \end{cases}, \quad (31)$$

where a_1, a_2, a_3, b_1, b_2 and b_3 are linear coefficients and u_t is a threshold to divide the subdomains of the piecewise function as shown in Fig. 8. Note that $\arccos_{\text{apx}}^\dagger(u) = \pi$ for $u \leq -1$ and $\arccos_{\text{apx}}^\dagger(u) = 0$ for $u \geq 1$. The optimal values for these coefficients and threshold are listed in Table II, which are obtained via a standard linear regression approach under the minimum mean square error (MMSE) criterion. This approximation is illustrated in Fig. 8, which shows minor difference between the approximated function and the original function. By applying (31) to (30), we are able to convert the integral into the form shown in (27). The solutions to the basic integrals in (27) can be found using (22) and (23):

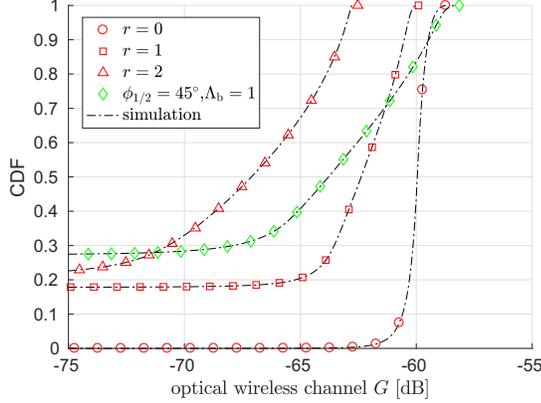
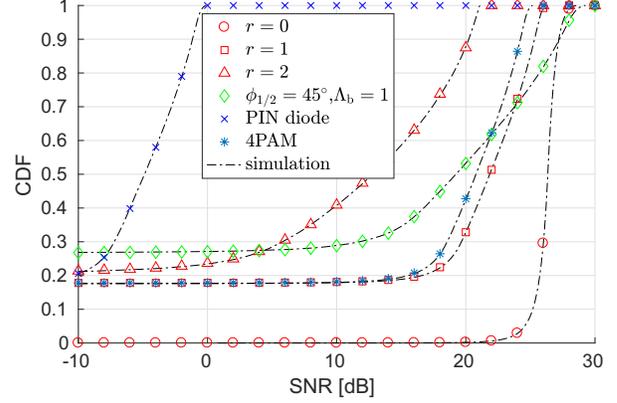
$$\begin{aligned} \int_u^v \frac{e^{-\frac{|\alpha-\mu_L|}{b_L}}}{2b_L} d\alpha &= \mathcal{C}_{u,v}, \quad \int_u^v \frac{e^{\pm \frac{\alpha-\mu_L}{b_L}}}{\sin \alpha} d\alpha = 2\mathcal{D}_{u,v}^{1,\pm 1}, \\ \int_u^v \frac{e^{\pm \frac{\alpha-\mu_L}{b_L}}}{\tan \alpha} d\alpha &= \mathcal{D}_{u,v}^{2,\pm 1} + \mathcal{D}_{u,v}^{0,\pm 1}. \end{aligned} \quad (32)$$

By inserting the solutions in (32) into (27) leads to the expression of (21). Now we go back to the the expression for $\mathbb{P}[G \leq T|\alpha]$ and use the approximation (31) to (29). The resultant piecewise function may equal to 1, $\frac{1_S \theta_3}{\pi}$, $\frac{a_1 \xi + b_1}{\pi} + \frac{1_S \theta_3}{\pi}$, $\frac{a_2 \xi + b_2}{\pi} + \frac{1_S \theta_3}{\pi}$ or $\frac{a_3 \xi + b_3}{\pi} + \frac{1_S \theta_3}{\pi}$ with various

values of α and T , as shown in Fig. 9. The next step is to calculate the average probability over the random variable α by $\mathbb{P}[G \leq T] = \int_0^{\frac{\pi}{2}} f_\alpha(\alpha) \mathbb{P}[G \leq T|\alpha] d\alpha$. This requires information of breakpoints of the piecewise function in terms of α threshold values, which correspond to the expressions concluded in (24). An illustration of these breakpoints is also presented in Fig. 9, where four boundary curves (break points) can be observed. The first curve is composed of α_1 and α_2 . It can be found that the value of $\mathbb{P}[G \leq T|\alpha]$ in the region on the right hand side of this curve equals one. The functions of α_1 and α_2 are obtained from solving the equation $\frac{1}{\pi} \arccos^\dagger(\xi) + \frac{1_S \theta_3}{\pi} = 1$ in conjunction with (28) with α as the unknown. The second curve corresponds to α_3 . The value of $\mathbb{P}[G \leq T|\alpha]$ in the region on the lower left hand side of this curve equals $\frac{1_S \theta_3}{\pi}$. The function of α_3 can be obtained by solving the equation $\frac{1}{\pi} \arccos^\dagger(\xi) = 0$ with α as the unknown. Due to the use of the approximation (31), the remaining two curves α_4, α_5 and α_6 divide the subdomains for the three linear functions. The functions of α_4, α_5 and α_6 can be calculated by solving the equations $\xi = \pm u_t$ with α as the unknown. Based on above information, we are able to conclude the values of the piecewise function $\mathbb{P}[G \leq T|\alpha]$ in each subdomains in Table III. Then it is intuitive to calculate $\mathbb{P}[G \leq T]$ by using this lookup table. For example, when $0 < T < T_1$, we can expand the integration as: $\mathbb{P}[G \leq T] = \int_0^{\alpha_3} f_\alpha(\alpha) \frac{1_S \theta_3}{\pi} d\alpha + \int_{\alpha_3}^{\alpha_6} f_\alpha(\alpha) \frac{1_S \theta_3 + a_3 \xi + b_3}{\pi} d\alpha + \int_{\alpha_6}^{\alpha_4} f_\alpha(\alpha) \frac{1_S \theta_3 + a_2 \xi + b_2}{\pi} d\alpha + \int_{\alpha_4}^{\alpha_1} f_\alpha(\alpha) \frac{1_S \theta_3 + a_1 \xi + b_1}{\pi} d\alpha + \int_{\alpha_1}^{\frac{\pi}{2}} f_\alpha(\alpha) d\alpha$, where each integral can be solved by using (21). Since the random blockage is independent from the

Table III: Lookup table for the function of $\mathbb{P}[G \leq T|\alpha]$

$T \in (0, T_1]$			$T \in (T_1, T_2]$			$T \in (T_2, T_3]$		
No.	range of α	$\mathbb{P}[G \leq T \alpha]$	No.	range of α	$\mathbb{P}[G \leq T \alpha]$	No.	range of α	$\mathbb{P}[G \leq T \alpha]$
1	$\alpha \in [0, \alpha_3]$	$\frac{1_S \theta_3}{\pi}$	6	$\alpha \in [0, \alpha_2]$	1	11	$\alpha \in [0, \alpha_2]$	1
2	$\alpha \in (\alpha_3, \alpha_6]$	$\frac{1_S \theta_3 + a_3 \xi + b_3}{\pi}$	7	$\alpha \in (\alpha_2, \alpha_5]$	$\frac{1_S \theta_3 + a_1 \xi + b_1}{\pi}$	12	$\alpha \in (\alpha_2, \alpha_1]$	$\frac{1_S \theta_3 + a_1 \xi + b_1}{\pi}$
3	$\alpha \in (\alpha_6, \alpha_4]$	$\frac{1_S \theta_3 + a_2 \xi + b_2}{\pi}$	8	$\alpha \in (\alpha_5, \alpha_4]$	$\frac{1_S \theta_3 + a_2 \xi + b_2}{\pi}$	13	$\alpha \in (\alpha_1, \frac{\pi}{2}]$	1
4	$\alpha \in (\alpha_4, \alpha_1]$	$\frac{1_S \theta_3 + a_1 \xi + b_1}{\pi}$	9	$\alpha \in (\alpha_4, \alpha_1]$	$\frac{1_S \theta_3 + a_1 \xi + b_1}{\pi}$	-	-	-
5	$\alpha \in (\alpha_1, \frac{\pi}{2}]$	1	10	$\alpha \in (\alpha_1, \frac{\pi}{2}]$	1	-	-	-


 Figure 10: CDF of optical wireless channel. If not specified the following default configurations are used: $r = 1$ m, $\phi_{1/2} = 60^\circ$ and $\Lambda_b = 0.1$. The remaining parameters are listed in Table I and IV.

 Figure 11: CDF of UL SNR. If not specified the following default configurations are used: $r = 1$ m, $\phi_{1/2} = 60^\circ$ and $\Lambda_b = 0.1$. The remaining parameters are listed in Table I and IV.

random orientation process, the final optical wireless channel CDF can be calculated using $F_G(T) = \mathcal{P}_{\text{rb}} + \mathcal{P}_{\text{los}} \mathbb{P}[G \leq T]$. Eventually, the calculation leads to the result of the first condition in (20). In conjunction with (24) and (25), the boundaries of the channel threshold T_1 , T_2 and T_3 can be obtained by solving the equations $\alpha_2 = \alpha_3$, $\alpha_4 = \alpha_5$ and $\alpha_1 = \alpha_2$ with T as the unknown, respectively. ■

B. Statistics of SNR

Corollary 1. Based on Proposition 1, the CDF of the UL SNR γ can be calculated as:

$$F_\gamma(T) = F_G \left(\frac{1}{2c_3} \left(c_2 T + \sqrt{c_2^2 T^2 + 4c_3 c_1 T} \right) \right), \quad (33)$$

where

$$c_1 = \frac{2\mathcal{K}_b \mathcal{T}_a}{R_L} + q\mathcal{M}^{2+\epsilon} I_{\text{bg}}, \quad c_2 = q\mathcal{M}^{2+\epsilon} \bar{p} \hat{H}(0),$$

$$c_3 = \frac{2\bar{p}^2 (2M-1) K T_s \mathcal{M}^2}{3(M-1) \sum_{k=0}^{K-1} \left| \sum_{l=-\infty}^{\infty} \hat{H} \left(\frac{k}{KT_s} - \frac{l}{T_s} \right) \right|^2}, \quad \text{with}$$

$$\hat{H}(f) = \int_{\lambda_{\min}}^{\lambda_{\max}} \mathcal{G}_{\text{of}}(\lambda) H_{\text{sp}}^2(f) H_{\text{pd}}(f, \lambda) H_{\text{led}}(f, \lambda) d\lambda. \quad (34)$$

Proof: The average signal photocurrent I_s in (13) can be calculated by:

$$I_s = \bar{p} G \int_{\lambda_{\min}}^{\lambda_{\max}} \mathcal{S}_{\text{led}}(\lambda) \mathcal{G}_{\text{of}}(\lambda) \mathcal{R}_{\text{pd}}(\lambda) d\lambda = \bar{p} G \hat{H}(0). \quad (35)$$

By inserting (13) into (9) and in conjunction with (35) and $H_{\text{ow}}(f, \lambda) = G$, the SNR expression can be rearranged as $\frac{c_3 G^2}{c_1 + c_2 G}$, where c_1 , c_2 and c_3 are as defined in (34). Thus, the CDF of the SNR can be rewritten as:

$$F_\gamma(T) = \mathbb{P}[\gamma \leq T] = \mathbb{P} \left[\frac{c_3 G^2}{c_1 + c_2 G} \leq T \right]$$

$$= \mathbb{P} [c_3 G^2 - c_2 T G - c_1 T \leq 0]. \quad (36)$$

By solving the inequality $c_3 G^2 - c_2 T G - c_1 T \leq 0$, the solution (33) can be obtained. ■

Remark. The closed form expressions (20) and (33) can be used as an analytical framework to analyse/optimize the configuration of system parameters. In addition, the derived statistics can be used to calculate various system performance metrics directly without using time consuming Monte Carlo simulations. Furthermore, it is also possible to generate random optical wireless channel/SNR samples using the rejection sampling technique for studies where random optical wireless channel/SNR samples are required.

In order to validate and investigate the derived statistics, we present a number of example results calculated using (20) and (33), and compare them with the corresponding Monte Carlo simulation results, as shown in Fig. 10 and Fig. 11. The agreement between the analytical results and the simulation results with various configurations validates the derivation and proves that the approximation (31) causes negligible errors. The results with red markers show that the deviation of the channel and SNR increases with an increase of horizontal offset r . In addition, the CDF curves are saturated at levels

Table IV: Simulation parameters II

Parameter	Symbol	Value
APD gain	\mathcal{M}	50
FFT block size	K	256
FoV	ψ_{FoV}	60°
LED cut-off frequency	$f_{c,\text{led}}$	35 MHz
LED half-power semiangle	$\phi_{1/2}$	60°
blocker radius	l_b	0.15 m
PAM order	M	2
symbol time	T_s	10 ns
terminal capacitance	C_T	12 pF
distance to windows	D_{win}	5 m
RB density	Λ_b	0.1 RB/m ²
UE to UB separation	r_{ub}	0.3 m

around 0.2 (consequence of link blockages) except for the case of $r = 0$. This implies that the UL transmission is more likely to be affected by link blockage and random device orientation with an increase of r . The results with green markers demonstrate that the link blockage probability increases with a higher value of random blocker density Λ_b . By using a narrower LED beam width $\phi_{1/2} = 45^\circ$, the link deviation of the channel and SNR also increases. The last two results shown in Fig. 11 with blue markers demonstrate that a PIN diode ($\mathcal{M} = 1$) with a small active area (7.1 m²) may not be sufficient to support LiFi UL transmissions, and an increase in modulation order leads to a higher PAPR.

V. COVERAGE PROBABILITY EVALUATION

In this section, we apply the analytical results presented in Section IV to evaluate the performance of the LiFi UL system in terms of coverage probability, which is defined as the probability that a UE in a LiFi network will achieve a threshold UL SNR. In this section, a random user position will be considered. Therefore, r is treated as a random variable and the CDF result presented in (33) should be denoted as $F_\gamma(T|r)$ here. By including the randomness of UE positions, we are able to include the AP association policies, AP layout and AP densities into play. Despite the necessity of one numerical integration, the numerical evaluation is still more efficient, convenient and tractable than implementing Monte Carlos simulations. Two AP association policies are considered. The first policy is called minimum distance association (minDA), which allows the UE to connect to the closest AP (lowest r). The second policy is called signal strength association (SSA), which lets the UE connect to the AP that provides the highest signal strength (highest SNR). The two policies are demonstrated in Fig. 12 (a). There are two APs near the considered UE. It can be observed that the UE is closer to AP 2 than AP 1 ($r_1 > r_2$). In the case of minDA, the UE will be associated with AP 2. On the other hand, AP 1 provides a higher SNR as the UL LED of the UE is better aligned with AP 1 ($\gamma_1 > \gamma_2$). In the case of SSA, the UE will be associated with AP 1.

A. Network with grid-based regular AP layout

In the practical scenario, a LiFi network may need to be built on top of an existing lighting network. This implies there might be constraints on the layout of LiFi APs. To achieve a uniform

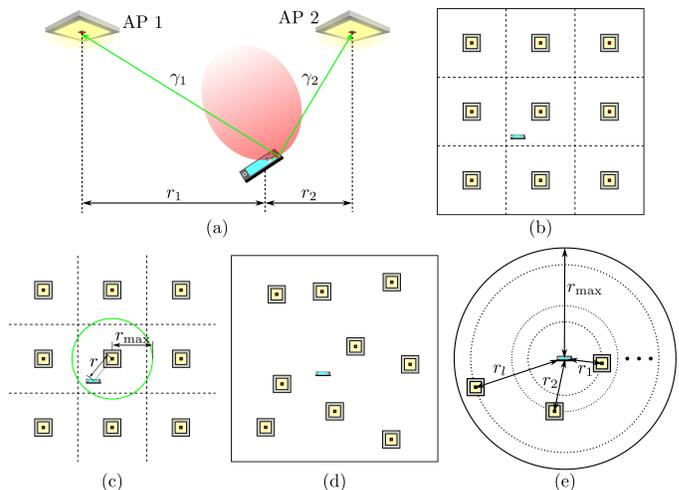


Figure 12: (a) Demonstration of different AP association policies. (b) Regular square-grid AP layout. (c) Random AP layout. (d) Geometry of coverage probability calculation with a regular grid-based AP layout. (e) Geometry of coverage probability calculation with random a AP layout.

illumination, a regular AP layout on a square grid is commonly used, as shown in Fig. 12 (b). In the case of minDA, the UE is covered by the nearest AP. Consequently, the statistics of the UEs in each cell are identical. Therefore, we consider the performance of a UE randomly distributed in one cell, as shown in Fig. 12 (c). For simplicity, we approximate the square cell by a circular cell with the same area. Considering a random node uniformly distributed within a circle with a radius of R , the PDF of the distance between the node and the circle centre τ is:

$$f_c^R(\tau) = \frac{2\tau}{R^2}. \quad (37)$$

Therefore, the PDF of the horizontal offset r can be calculated by $f_{r,c}^{R_c}(r)$ where R_c is the radius of the circular cell, which can be obtained from the AP density Λ_a by $R_c = 1/\sqrt{\pi\Lambda_a}$. Thus, the coverage probability can be calculated by averaging over r as:

$$\begin{aligned} \mathcal{P}_c &= 1 - \int_0^{R_c} f_{r,c}^{R_c}(r) F_\gamma(T|r) dr \\ &= 1 - \frac{2}{R_c^2} \int_0^{R_c} r F_\gamma(T|r) dr. \end{aligned} \quad (38)$$

B. Network with random AP layout

In some indoor environments, uniform lighting is not required and the layout of APs might exhibit some randomness, as shown in Fig. 12 (d). In order to take these scenarios into account, we also consider a LiFi network with a random AP layout following a homogeneous PPP. In this case, we consider a polar coordinate system with the UE position as the origin, as shown in Fig. 12 (e). Assuming there are N_a APs randomly distributed within a circle with a radius of r_{max} . In the case of minDA, the r equals the horizontal distance between the UE and the closest AP. Therefore, the PDF of r can be found as [36]: $f_{\text{PPP}}^{\text{1st}}(r) = 2\pi\Lambda_a r \exp(-\Lambda_a \pi r^2)$ where Λ_a is the AP

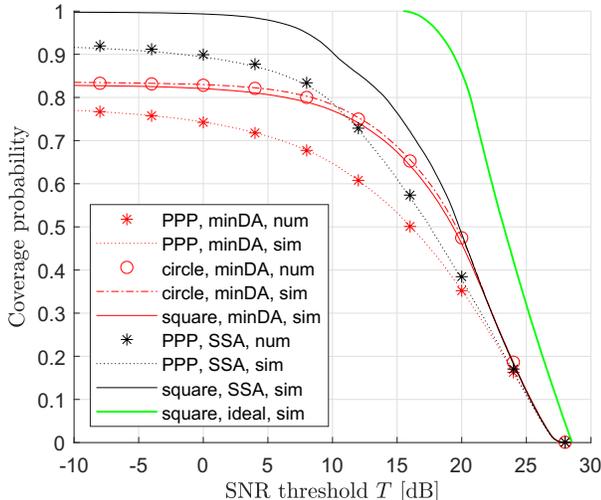


Figure 13: Coverage probability of various AP layout and AP association. The notation ‘num’ means numerical result and ‘sim’ means Monte Carlo simulation results.

spatial density. Thus, the coverage probability can be found as:

$$\begin{aligned} \mathcal{P}_c &= 1 - \int_0^{r_{\max}} \mathfrak{f}_{\text{PPP}}^{\text{1st}}(r) F_\gamma(T|r) dr \\ &= 1 - 2\pi\Lambda_a \int_0^{r_{\max}} r e^{-\Lambda_a \pi r^2} F_\gamma(T|r) dr. \end{aligned} \quad (39)$$

In the case of SSA, the UE can be associated to any one of the N_a APs. Due to the randomness in AP position, device orientation and link blockage, the UL SNRs corresponding to each AP are independent and identically distributed (i.i.d.) random variables $\tilde{\gamma}$. In conjunction with (37), the CDF of $\tilde{\gamma}$ can be calculated by:

$$\begin{aligned} F_{\tilde{\gamma}}(T) &= \int_0^{r_{\max}} \mathfrak{f}_c^{r_{\max}}(r) F_\gamma(T|r) dr \\ &= \frac{2}{r_{\max}^2} \int_0^{r_{\max}} r F_\gamma(T|r) dr. \end{aligned} \quad (40)$$

According to the theory of order statistics, the maxima of $\tilde{\gamma}$ among the N_a APs can be calculated by $\{F_{\tilde{\gamma}}(T)\}^{N_a}$ [37]. Since the number of APs within the circle with the radius of r_{\max} follows a Poisson distribution with a PDF of $\mathbb{P}[N_a = l] = e^{-\Lambda_a \pi r_{\max}^2} (\Lambda_a \pi r_{\max}^2)^l / l!$. Eventually, by averaging over N_a , the coverage probability can be calculated as:

$$\begin{aligned} \mathcal{P}_c &= 1 - \sum_{l=0}^{\infty} \mathbb{P}[N_a = l] \{F_{\tilde{\gamma}}(T)\}^l \\ &= 1 - \exp\left(2\pi\Lambda_a \int_0^{r_{\max}} r F_\gamma(T|r) dr - \Lambda_a \pi r_{\max}^2\right). \end{aligned} \quad (41)$$

In theory, r_{\max} should be $\hat{z} \tan \psi_{\text{FoV}}$, but $r_{\max} \geq 5$ is sufficient for obtaining accurate results.

C. Results and discussions

In the following results, most of the system parameters are listed in Table I and IV. In addition, an AP density of

$\Lambda_a = 0.08 \text{ AP/m}^2$ is considered as an example. In Fig. 13, the numerical results with various AP layouts and AP association policies calculated using (38), (39) and (41) are presented along with the Monte Carlo simulation results. Furthermore, the simulation results of the systems with square AP layouts under minDA and SSA policies are also presented. In particular, a simulation result in an ideal condition without the effects of link blockage and random device orientation (device facing straight upward) is also included for comparison. Considering an SNR threshold of 10 dB, the LiFi UL system in the ideal condition achieves a coverage probability of 100%. In contrast, the remaining systems under the effects of link blockage and random device orientation achieve coverage probabilities in the range of 65% to 90%. This means a performance penalty of 10% to 35% in terms of coverage probability. Comparing the results with different AP association policies, the systems with SSA (black) achieves 15% to 20% higher coverage probability than those achieved by systems with minDA (red) with a 10 dB threshold. This is because the nearest AP does not necessarily provide the strongest desired signal due to the undesired LED orientation in many conditions. Comparing the systems with various AP layouts, the systems with regular AP layouts (circular, square) outperform those with irregular AP layouts (PPP) by 10% to 15% in terms of coverage probability with a 10 dB threshold. Also note that the systems with circular and square AP layouts under the minDA achieve similar coverage probabilities. This indicates that using a circular cell to approximate the square cell is valid in Section V-A.

Next, we consider the effects of varying a number of parameters on the performance of the LiFi UL transmission. Fig. 14 shows the coverage probability varying with (a) the transmitter half-power semiangle $\phi_{1/2}$, (b) detector FoV ψ_{FoV} , (c) AP density Λ_a and (d) RB density Λ_b . The results with a threshold of $T = 10$ dB are presented as examples. The presented results include the cases with various AP layouts and AP association policies calculated using (38), (39) and (41). The simulation result for square AP layout under SSA policy is also included as the corresponding numerical result is not available. Fig. 14 (a) shows that the coverage probability improved by 15% to 30% with an increase of $\phi_{1/2}$ from 30° to 60°. This is because the LED is less likely to be aligned with an AP under the effects of random orientation. Therefore, a large $\phi_{1/2}$ could improve the channel gain when the link is not well-aligned and enhance the channel reliability against random device orientation.

Fig. 14 (b) shows that the coverage probability increases with an increase of ψ_{FoV} for small values of ψ_{FoV} . An excessively narrow FoV limits the AP coverage region, which significantly increases the probability that the UE is out of the FoV of any neighbouring AP receiver (enter the ‘dark zone’). The coverage probability reaches a peak with a ψ_{FoV} in the range of 40° to 60°, and start to slightly decrease with a further increase of ψ_{FoV} . This is because the ‘dark zone’ is almost eliminated when ψ_{FoV} is sufficiently large. Further increases in ψ_{FoV} become pointless but decrease the gain from the optical concentrator g_c .

Fig. 14 (c) shows that the coverage probability increases with the AP density Λ_a . Note that AP density can also

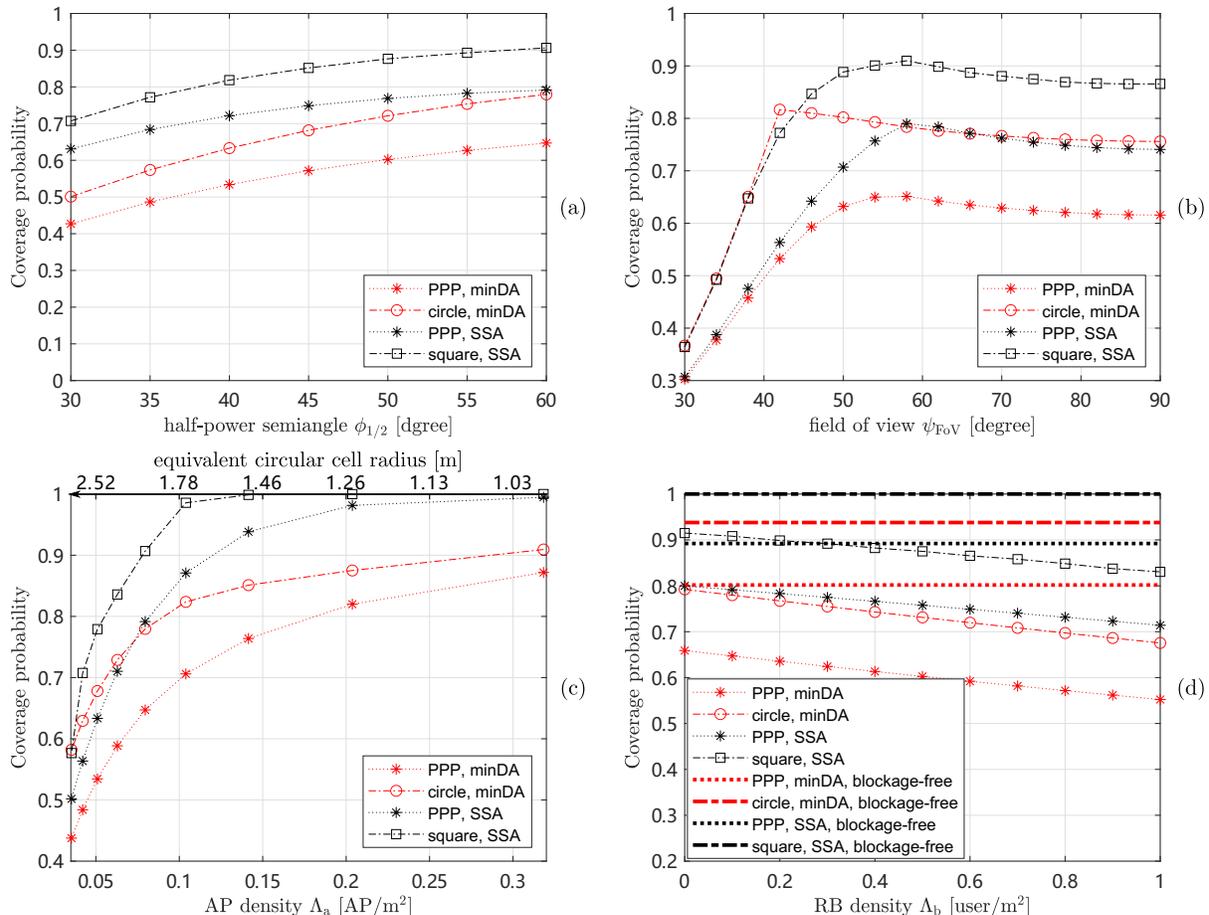


Figure 14: (a) Coverage probability varies with transmitter half-power semiangle $\phi_{1/2}$. (b) Coverage probability varies with receiver FoV ψ_{FoV} . (c) Coverage probability varies with AP density Λ_a . (d) Coverage probability varies with RB density Λ_b .

be interpreted as a equivalent circular cell radius, which is labelled on the top of Fig. 14 (c). A smaller Λ_a leads to a longer average horizontal link distance r . As demonstrated in Fig. 12 (a), the channel deviation and the link blockage probability increases significantly with r . Consequently, the coverage probability drops significantly with a decrease of Λ_a . Therefore, the AP density should be high to shorten the average value of r . It can be observed that an AP density of $\Lambda_a = 0.1$ AP/m² (1.75 m cell radius) leads to a coverage probability of 70% to 100%. When the AP density drops to $\Lambda_a = 0.05$ AP/m² (2.5 m cell radius), the coverage probability decreases to the range of 50% to 80%.

Fig. 14 (d) shows that the coverage probability decreases with an increase of RB density Λ_b . In addition, the coverage probability without the effects of link blockage is also depicted for comparison. The gap between the results with and without the effects of link blockage indicate the performance penalty caused by link blockage. The penalty is in the range of 10% to 30% in terms of coverage probability. Note that the gap between results at $\Lambda_b = 0$ reflects the penalty caused by the UB, which is in the range of 10% to 15% in terms of coverage probability. It can be observed that the coverage probability decreases linearly by 10% to 15% with an increase of Λ_b from 0 to 1 user/m². When the random blocker density is not

significant, UB is the dominant cause of link blockage.

VI. CONCLUSIONS

In this paper, the performance of a wireless IR-based LiFi UL transmission under the effects of link blockage and random device orientation is investigated. We have extended the PAM-SCFDE framework to include more practical factors in the model. The properties of the receiver noise in the UL scenario are evaluated and discussed. In particular, we have developed closed-form expression for the statistics of the optical wireless channel and SNR under the effects of link blockage and random device orientation. We have used the developed analytical expressions to evaluate the coverage probability of the LiFi UL transmission with various AP layouts and AP association policies. The results show that the link blockage and random device orientation may cause a UL transmission performance penalty of 10% to 35% in terms of coverage probability. To achieve better coverage probability, a wide transmitter half-power semiangle of 60° and a receiver FoV in the range of 40° to 60° are suitable choices. Furthermore, the link blockage issue causes a significant system coverage probability decrease by 10% to 30%.

In the current study, the IR-based LiFi UL transmission from a single LED to a single detector is considered. The results

have revealed the significant performance degradation caused by link blockage and random device orientation. In future studies, UL transmission systems with multiple LEDs/detectors can be considered to overcome this issue and to improve the link reliability using the diversity gain. Furthermore, the current analysis can also be extended to study the UL multiple access schemes by considering statistics of co-channel interference.

ACKNOWLEDGMENT

Professor Haas acknowledges the financial support from the Wolfson Foundation, the EPSRC UK under Established Career Fellowship grant EP/R007101/1.

REFERENCES

- [1] M. S. Islam, R. X. Ferreira, X. He, E. Xie, S. Videv, S. Viola, S. Watson, N. Bamiedakis, R. V. Pentyl, I. H. White, A. E. Kelly, E. Gu, H. Haas, and M. D. Dawson, "Towards 10 Gb/s Orthogonal Frequency Division Multiplexing-based Visible Light Communication using a GaN Violet micro-LED," *Photon. Res.*, vol. 5, no. 2, pp. A35–A43, Apr 2017.
- [2] H. Haas, L. Yin, Y. Wang, and C. Chen, "What is LiFi?" *J. Lightw. Technol.*, vol. 34, no. 6, pp. 1533–1544, Mar. 2016.
- [3] L. Yin and H. Haas, "Physical-Layer Security in Multiuser Visible Light Communication Networks," *IEEE J. Sel. Areas Commun.*, vol. 36, no. 1, pp. 162–174, Jan. 2018.
- [4] C. Chen, D. A. Basnayaka, and H. Haas, "Downlink Performance of Optical Attocell Networks," *J. Lightw. Technol.*, vol. 34, no. 1, pp. 137–156, Jan. 2016.
- [5] P. H. Pathak, X. Feng, P. Hu, and P. Mohapatra, "Visible Light Communication, Networking, and Sensing: A Survey, Potential and Challenges," *IEEE Commun. Surveys Tutorials*, vol. 17, no. 4, pp. 2047–2077, Fourthquarter 2015.
- [6] P. Perez-Nicoli, F. Silveira, X. Zhang, and A. Amara, "Uplink Wireless Transmission Overview in Bi-directional VLC Systems," in *Proc. IEEE International Conference on Electronics, Circuits and Systems (ICECS)*, Monte Carlo, Monaco, Dec. 2016, pp. 588–591.
- [7] F. Duvnjak, J. Ozegovic, and A. Kristic, "Heterogeneous Wi-Fi and VLC (RF-optical) Wireless Access Architecture," in *23rd Int. Conf. on Software, Telecommun. and Comput. Networks*, Split, Croatia, Sep. 2015, pp. 310–314.
- [8] Y. Wang, N. Chi, Y. Wang, L. Tao, and J. Shi, "Network Architecture of a High-Speed Visible Light Communication Local Area Network," *IEEE Photonics Technol. Lett.*, vol. 27, no. 2, pp. 197–200, Jan. 2015.
- [9] Y. Wang, Y. Shao, H. Shang, X. Lu, Y. Wang, J. Yu, and N. Chi, "875-Mb/s Asynchronous Bi-directional 64QAM-OFDM SCM-WDM Transmission over RGB-LED-based Visible Light Communication System," in *Optical Fiber Commun. Conf. and Exposition and the Nat. Fiber Optic Engineers Conf.*, Anaheim, CA, USA, Mar. 2013, pp. 1–3.
- [10] G. Cossu, A. Wajahat, R. Corsini, and E. Ciaramella, "5.6 Gbit/s Downlink and 1.5 Gbit/s Uplink Optical Wireless Transmission at Indoor Distances (≥ 1.5 m)," in *2014 The European Conference on Optical Communication (ECOC)*, 2014, pp. 1–3.
- [11] G. Cossu, R. Corsini, and E. Ciaramella, "High-Speed Bi-directional Optical Wireless System in Non-Directed Line-of-Sight Configuration," *J. Lightw. Technol.*, vol. 32, no. 10, pp. 2035–2040, May 2014.
- [12] T. Bui and S. Kiravittaya, "Demonstration of Using Camera Communication Based Infrared LED for Uplink in Indoor Visible Light Communication," in *2016 IEEE Sixth International Conference on Communications and Electronics (ICCE)*, 2016, pp. 71–76.
- [13] E. S. S. Edirisinghe, P. H. R. S. S. Karunarathna, D. M. T. B. Dissanayake, and G. M. R. I. Godaliyadda, "Design and Implementation of a Bi-directional Visible Light Communication System," in *2015 IEEE 10th International Conference on Industrial and Information Systems (ICIIS)*, 2015, pp. 519–524.
- [14] O. Narmanlioglu, B. Turan, R. C. Kizilirmak, S. C. Ergen, and M. Uysal, "SC-FDE Based MIMO Uplink Transmission Over Infrared Communication Channels," in *2018 IEEE 88th Vehicular Technology Conference (VTC-Fall)*, 2018, pp. 1–5.
- [15] A. A. Purwita, C. Chen, M. Safari, and H. Haas, "Cyclic-Prefixed System with PAM using DFE and THP for Uplink Transmission in LiFi," in *ICC 2019 - 2019 IEEE International Conference on Communications (ICC)*, 2019, pp. 1–6.
- [16] D. Tagliaferri and C. Capsoni, "High-speed Wireless Infrared Uplink Scheme for Airplane Passengers' Communications," *Electronics Letters*, vol. 53, no. 13, pp. 887–888, 2017.
- [17] C. Chen, R. Bian, and H. Haas, "Omnidirectional Transmitter and Receiver Design for Wireless Infrared Uplink Transmission in LiFi," in *2018 IEEE International Conference on Communications Workshops (ICC Workshops)*, 2018, pp. 1–6.
- [18] M. T. Alresheedi, A. T. Hussein, and J. M. H. Elmighani, "Uplink Design in VLC Systems with IR Sources and Beam Steering," *IET Communications*, vol. 11, no. 3, pp. 311–317, 2017.
- [19] O. Z. Alsulami, M. T. Alresheedi, and J. M. H. Elmighani, "Infrared Uplink Design for Visible Light Communication (VLC) Systems with Beam Steering," in *2019 IEEE International Conference on Computational Science and Engineering (CSE) and IEEE International Conference on Embedded and Ubiquitous Computing (EUC)*, 2019, pp. 57–60.
- [20] T. Bui and M. Biagi, "TDMA-Like Infrared Uplink with Multi-Faces Photodiode Access Points," in *2019 IEEE International Conference on Communications Workshops (ICC Workshops)*, 2019, pp. 1–5.
- [21] A. Nuwanpriya, S. W. Ho, J. A. Zhang, A. J. Grant, and L. Luo, "PAM-SCFDE for Optical Wireless Communications," *J. Lightw. Technol.*, vol. 33, no. 14, pp. 2938–2949, Jul. 2015.
- [22] F. Pincaldi, G. M. Vitetta, R. Kalbasi, N. Al-Dhahir, M. Uysal, and H. Mheidat, "Single-carrier Frequency Domain Equalization," *IEEE Signal Processing Magazine*, vol. 25, no. 5, pp. 37–56, 2008.
- [23] Yuan-Pei Lin and See-May Phoong, "BER Minimized OFDM Systems with Channel Independent Precoders," *IEEE Trans. Signal Process.*, vol. 51, no. 9, pp. 2369–2380, Sep. 2003.
- [24] J. Proakis, *Digital Communications*, ser. McGraw-Hill series in electrical and computer engineering : communications and signal processing. McGraw-Hill, 2001.
- [25] E. F. Schubert, *Light-Emitting Diodes*, 2nd ed. Cambridge University Press, 2006.
- [26] S. S. D. HAMAMATSU PHOTONICS K.K., "Characteristics and Use of Si APD (Avalanche Photodiode)," Tech. Rep., May 2004.
- [27] N. S. Kopeika and J. Bordonaga, "Background Noise in Optical Communication Systems," *Proceedings of the IEEE*, vol. 58, no. 10, pp. 1571–1577, Oct 1970.
- [28] J. M. Kahn and J. R. Barry, "Wireless Infrared Communications," *Proc. IEEE*, vol. 85, no. 2, pp. 265–298, Feb. 1997.
- [29] I. E. Commission et al., "Photobiological Safety of Lamps and Lamp Systems," *Geneva: IEC*, vol. 62471, 2006.
- [30] J. M. Kahn and J. R. Barry, "Wireless Infrared Communications," *Proc. IEEE*, vol. 85, no. 2, pp. 265–298, Feb. 1997.
- [31] J. Barry, J. Kahn, W. Krause, E. Lee, and D. Messerschmitt, "Simulation of Multipath Impulse Response for Indoor Wireless Optical Channels," *IEEE J. Sel. Areas Commun.*, vol. 11, no. 3, pp. 367–379, Apr. 1993.
- [32] H. Schulze, "Frequency-Domain Simulation of the Indoor Wireless Optical Communication Channel," *IEEE Trans. Commun.*, vol. 64, no. 6, pp. 2551–2562, June 2016.
- [33] M. D. Soltani, A. A. Purwita, Z. Zeng, H. Haas, and M. Safari, "Modeling the Random Orientation of Mobile Devices: Measurement, Analysis and LiFi Use Case," *IEEE Trans. Commun.*, vol. 67, no. 3, pp. 2157–2172, Mar. 2019.
- [34] K. Dong, X. Liao, and S. Zhu, "Link Blockage Analysis for Indoor 60GHz Radio Systems," *Electronics Letters*, vol. 48, no. 23, pp. 1506–1508, Nov. 2012.
- [35] F. Firyaguna, J. Kibilda, C. Galiotto, and N. Marchetti, "Coverage and Spectral Efficiency of Indoor mmWave Networks with Ceiling-Mounted Access Points," in *IEEE Global Commun. Conf.*, Singapore, Singapore, Dec. 2017, pp. 1–7.
- [36] M. Haenggi, "On Distances in Uniformly Random Networks," *IEEE Trans. Inf. Theory*, vol. 51, no. 10, pp. 3584–3586, Oct. 2005.
- [37] H. A. David and H. N. Nagaraja, *Order Statistics*. John Wiley and Sons, 2003.



Cheng Chen received the B.Eng. degree in electronic and electrical engineering from the University of Strathclyde, Glasgow, U.K., in 2011, the M.Sc. degree in communications and signal processing from the Imperial College, London, U.K., in 2012, and the Ph.D. degree in electrical engineering from the University of Edinburgh, Edinburgh, U.K., in 2017. He is currently employed as a Research Associate with the Li-Fi Research and Development Centre, the University of Strathclyde and is working in the field of visible light communications and LiFi

networks. His main research interests are in the areas of optical wireless communication, visible light communication, and wireless communication for 6G. He has authored or coauthored 30 publications in these areas.



Harald Haas FREng FRSE FIEEE FIET received the Ph.D. degree from The University of Edinburgh in 2001. He is a Distinguished Professor of Mobile Communications at The University of Strathclyde/Glasgow and the Director of the LiFi Research and Development Centre. Prof Haas is the Initiator, co-founder and Chief Scientific Officer of pureLiFi Ltd.. He has co-authored more than 550 conference and journal papers, including papers in Science and Nature Communications. Haas' main research interests are in optical wireless communica-

tions. He introduced LiFi to the public at an invited TED Global talk in 2011. Subsequently, LiFi was listed among the 50 best inventions in TIME Magazine in 2011. He gave a second TED Global lecture in 2015 on the use of solar cells as LiFi data detectors and energy harvesters. In 2016, he received the Outstanding Achievement Award from the International Solid State Lighting Alliance. In 2019 he was recipient of IEEE Vehicular Society James Evans Avant Garde Award. In 2017 he received a Royal Society Wolfson Research Merit Award.



Dushyantha A. Basnayaka (S'11–M'12–SM'18) is an Assistant Professor of Electrical and Electronics Engineering at Dublin City University (DCU), Dublin, Ireland. Prior to that he was with the Institute for Digital Communication at University of Edinburgh, Edinburgh, UK since 2013. He received the B.Sc.Eng (1st Class Hons) and the Ph.D. degree in Electrical and Electronics Engineering respectively in 2006 and 2012. His current research broadly lies at the intersection of Wireless Communication and Applied Electromagnetism, and currently focuses on

physical layer aspects for beyond-5G wireless communication. He holds patents in key areas of wireless communication, and is also the recipient of the best paper award at Institute for Electrical and Electronics Engineers (IEEE) Vehicular Technology Conference (VTC-Spring) 2015 - the flagship conference of IEEE Vehicular Technology Society. Prof. Basnayaka has also held a full-time appointment in the Department of Global Investment Operations at Aberdeen Standard Investment (ASI), Edinburgh, UK. ASI is the largest active asset manager in the UK. He is a Senior Member of IEEE, USA - the largest professional organisation in the world for the advancement of science and technology.



Ardimas Andi Purwita (S'15) received the B.S. and M.Sc. degrees in electrical engineering from the Institut Teknologi Bandung, Bandung, Indonesia, in 2011 and 2014, respectively. He is currently pursuing the Ph.D. degree with The University of Edinburgh, Edinburgh, U.K. He was with the School of Information Science, Japan Advanced Institute of Science and Technology, in 2015, as a Researcher. His current research interests include channel coding, optical wireless communication, hybrid Wi-Fi-LiFi, LiFi standard (IEEE 802.11bb), and cloud

computing.



Xiping Wu received the Ph.D. degree from The University of Edinburgh in 2015. From 2015 to 2018, he held a Post-Doctoral Fellowship with The University of Edinburgh, funded by the British EPSRC (Engineering and Physical Sciences Research Council). From 2019 to 2020, he was a Research Fellow at University of Oxford, funded by the European Commission Horizon 2020 (H2020). He is currently an Assistant Professor at School of Electrical and Electronic Engineering, University College Dublin. His main research interests are in the areas of 6G

mobile communications, optical wireless communications (OWC), hybrid OWC and RF networks, and the Internet of Things. He has authored or coauthored over 50 publications in these areas.